THE JOURNAL OF PHYSICAL CHEMISTRY C
A JOURNAL OF THE AMERICAN CHEMICAL SOCIETY

pubs.acs.org/JPCC
Article

DFT Investigation of X_{55} (X = Ni, Pd, and Pt) Clusters on Ultrathin Supported MgO Films: Evidence of Oxygen Spillover and Relevance for Catalytic Model Studies

Mirali Jahangirzadeh Varjovi* and Sergio Tosoni*

Cite This: J. Phys. Chem. C 2024, 128, 21331−21342
Read Online

ACCESS | Metrics & More | Article Recommendations | Supporting Information

ABSTRACT: The adsorption of X_{55} (X = Ni, Pd, and Pt) nanoclusters is simulated by using first-principles methods on MgO(100) and on a MgO monolayer supported on Ag(100), considering the presence of interfacial oxygen. On both the free-standing MgO surface and MgO/Ag, all clusters exhibit robust adhesion and negative charge transfer. *Ab initio* molecular dynamics calculations at 200 K demonstrate the stability of the X_{55} nanoparticles on the MgO/Ag support. The presence of oxygen segregated at the MgO-Ag interface significantly stabilizes the adsorbed X_{55} clusters, particularly Ni_{55}, and induces electron withdrawal. Thermodynamically favorable reverse oxygen spillover from the interface to the adsorbed particles occurs for Ni, Pd, and Pt, altering the particles' charge polarity. Simulation of higher oxygen loading at the surface results in spontaneous spillover, with some oxygen atoms segregating back at the MgO/Ag interface, which can thus act as a buffer during oxidation processes on the metal nanoparticles. Our computational results, which provide detailed insights into the adsorption of X_{55} nanoclusters on various supports, efficiently present a wide range of scenarios and hypotheses, serving as realistic models for experimental studies.

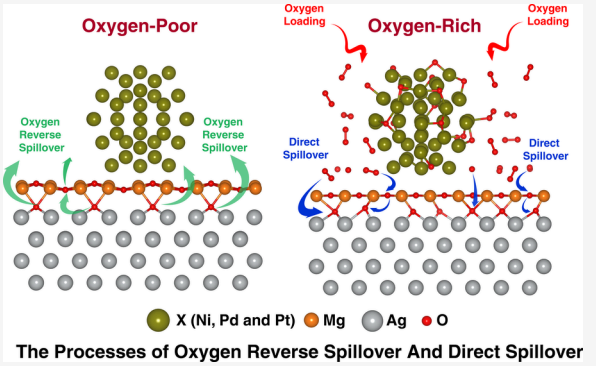

The Processes of Oxygen Reverse Spillover And Direct Spillover

1. INTRODUCTION

Catalysis is the key to most industrial chemical processes, which are fundamental to the welfare and wide availability of goods in contemporary society,[1] and its relevance can only increase during the transition toward sustainable and efficient chemical cycles bolstered by renewable energy sources. Catalytic devices currently in use are predominantly within the realm of heterogeneous catalysis,[2] where the prototype of a catalyst is often a metal particle comprising hundreds or even thousands of atoms dispersed on a carbonaceous or oxidic support.[3,4] The properties of the catalyst are primarily determined by the chemical nature of the metal,[5] the interaction with the support,[6−12] and the size and dispersion of the nanoparticles,[13] as seen for instance in the paradigmatic case of small Au aggregates.[14−16] Given the complex morphology of real catalysts and the highly dynamic, multifactor-dependent environment of its properties, it is interesting to complement applied studies in catalysis with fundamental research dedicated to unraveling the structure−activity relationships in model systems under controlled reaction conditions, recurring to high-definition electron microscopies.[17] The idea to extend the use of electron scanning techniques to the realm of nonconducting, yet catalytically relevant, oxide surfaces spurred significant interest in the growth and characterization of oxide ultrathin films on metal supports, as the minimal thickness of these films permits electron tunneling between the metal support and the metallic tip through the insulating film.[18] However, the charge transfer phenomenon enabled by the tunneling effect turned out to infer peculiar chemical and physical properties to these ultrathin oxide films, which eventually emerged as a promising new type of support for catalytic metallic nanoparticles.[19]

Among many possible oxide films, magnesium oxide (MgO) attracted remarkable attention due to its good lattice match with metal supports such as silver (Ag) or molybdenum (Mo), enabling epitaxial growth of ordered films.[20] Additionally, it has been reported that the electron transfer via tunneling through the MgO film induced the formation of negatively charged and highly reactive subnanometric Au particles.[21,22] Compared with other oxides, MgO provides a relatively chemically inert support, ensuring that the adsorbed metal nanoparticles remain largely unaffected by significant interfacial structural reconstruction. However, an important factor must not be overlooked: as shown by combining Scanning Tunneling Microscopy (STM) imaging with Xray Photoemission Spectroscopy (XPS) measurements and Density Functional Theory (DFT) calculations, when MgO

Received: June 25, 2024
Revised: September 16, 2024
Accepted: October 28, 2024
Published: December 8, 2024

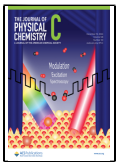

is grown on Ag through the on-site oxidation process of Mg, a non-negligible amount of oxygen becomes trapped at the MgO/Ag interface, significantly impacting crucial properties such as the work function and charge transfer.[23] An optimal concentration of interfacial oxygen, reaching as high as 25% of the Ag surface hollow sites under growth conditions, was estimated using *ab initio* thermodynamics.[23] Moreover, it cannot be excluded that interfacial oxygen species are not uniformly distributed but tend to segregate at the borders of the MgO islands.[24] Notably, the spontaneous oxygenation of non-noble metals, such as Ni ultrasmall aggregates on MgO/Ag, has been reported even under ultrahigh vacuum conditions. This observation underscores the potential for interfacial oxygen to diffuse across the surface and directly participate in chemical reactions with adsorbed metallic species.[25] Larger Ni adducts have also been found to activate probe molecules such as CO.[26] This phenomenon merits further investigation, especially given the catalytic significance of Ni and other group-10 transition metals in catalysis[27−35] particularly when they experience partial oxidation.[36,37] It is also worth mentioning that, in several cases, the catalytic active species turned out to be a thin metal oxide layer coating the group-10 metal nanoparticles.[38−40] This fact highlights how the availability of mobile interfacial oxygen species could enhance the relevance of these types of systems as model catalysts, effectively mimicking the real active phases. Hence, we conduct a comparative study involving relatively large nanoclusters of X_{55} (X = Ni, Pd, and Pt) each with a diameter exceeding 1 nm, supported on various substrates, including free-standing MgO and MgO monolayers on Ag with and without interfacial oxygen. This enables us to compare the physical and chemical properties of these particles on different supports.

The modeling of nanoparticles on metal-supported oxides presents significant challenges. On one hand, computationally intensive methodologies based on genetic algorithms[41,42] or machine-learning accelerated techniques[43−45] allow for scanning over many possible structures of limited size,[46] compared to what can be done for their gas-phase homologous.[47] On the other hand, the size problem can be overcome by resorting to periodic models of extended metal-oxide interfaces, but at the expense of losing the description of the border regions of the supported nanoparticles.[48] Otherwise, larger clusters on MgO have been studied adopting interatomic potentials.[49] The complex topic of bridging gaps in the multiscale modeling of catalytic systems has been widely reviewed elsewhere.[50] In the present study, our aim is to overcome this problem by modeling particles that fall within the scalable regime and exhibit high stability.[51] The remainder of the paper is organized as follows: the Computational Methodology is provided in Section 2. Section 3 presents the results for the structural, electronic, and magnetic features of the examined systems, and finally, we conclude our findings in Section 4.

2. COMPUTATIONAL DETAILS

In the present study, all first-principle calculations were conducted within the framework of spin-polarized Density Functional Theory (DFT),[52,53] as implemented in the Vienna Ab initio Simulation Package (VASP).[54−57] The exchange-correlation potential was parametrized using the Perdew−Burke−Ernzerhof (PBE)[58] functional within the generalized gradient approximation (GGA). The projector-augmented wave (PAW)[59] approach was utilized to portray the pseudopotentials of the elements. To expand the electronic wave function, a plane-wave basis set with a kinetic cutoff energy of 520 eV was utilized and a vacuum layer of ∼20 Å was included in the nonperiodic dimension of all calculations involving clusters on different supports to hinder the unrealistic interactions among adjacent images. The electronic relaxation convergence threshold between consecutive steps in total energy calculations was less than 10^{-5} eV. The truncation criteria for structural optimization (ionic loops and lattice constants) were set to 0.01 eV/Å. Brillouin zone (BZ) sampling was performed using a Γ-centered 8 × 8 × 1 uniform *k*-point mesh for the relaxation of the MgO (100) monolayer and Ag(100).[60] To obtain the optimized structures of the clusters on different supports, VASP-Γ and 1 × 1 × 1 *k*-point grids were employed, as justified by the large supercells. To determine the net charge transfer between the clusters and their support, the Bader technique was utilized.[61] Additionally, long-range dispersion effects were taken into account based on the D3 approach from Grimme, which incorporates the Becke-Johnson damping function.[62,63] All calculations started from the same initial guess for the magnetic configuration: a singlet state for Mg, O, and Ag (when present) and a triplet state for Ni, Pd, and Pt. The magnetic configuration was left to change during the self-consistent field iterations. *Ab initio* molecular dynamics (AIMD) simulations were performed using a microcanonical ensemble approach at a constant temperature (200 K) for a total simulation duration of 5 ps, employing a time step of 1 fs. The adsorption energy of the nanoclusters, E_{ads} can be defined as follows:

$$E_{ads} = E_{X55/Support} - E_{X55} - E_{Support} \quad (1)$$

and for the case of high oxygen loading (Section 3.3)

$$E_{ads} = E_{X55/Support/nO} - E_{X55} - E_{Support} - nE_{O2}/2 \quad (2)$$

where $E_{X55/Support}$ and $E_{X55/Support/nO}$ represent the energy of the examined systems in the absence and presence of oxygen loadings, respectively, E_{X55}, $E_{Support}$ and E_{O2} denote the total energies of gas-phase nanoclusters, the support, and the O_2 molecules, respectively, and 'n' indicates the number of oxygen loading atoms.

3. RESULTS AND DISCUSSION

In this study, we concentrate on the high-symmetry configuration of icosahedron (Ih) for 55-atom size clusters, denoted as X_{55} clusters (X = Ni, Pd, and Pt).[64] Ih-X_{55} clusters belong to the family of so-called magic-size clusters, characterized by compact atomic shells and highly stable configurations. Ih-X_{55} clusters have a size large enough to exhibit electronic structures akin to bulk materials yet small enough to enable thorough theoretical analysis. The icosahedral shape has been identified as the global minimum for Ni_{55} and Pd_{55}.[65] However, a later work proved that the icosahedral shape is the second most stable structure for 55-atom Pd clusters and attributed a more distorted structure as the global minimum for Pt_{55}.[66] In this study, all static relaxations for the supported X_{55} clusters were initiated from the icosahedral shape, allowing all atoms to relax freely during the simulation. To simulate the MgO/Ag interface, we assumed a coincidence between MgO(100) $\sqrt{2} \times \sqrt{2}$ R45 and Ag(100) (1 × 1) structures. Oxygen atoms were placed in registry with the underlying Ag atoms, while the Mg atoms occupied hollow positions. The Ag support is modeled with a 4-layer thick slab, where the atoms from the bottom layer are fixed in their bulk positions, while the positions of all other atoms are relaxed. The adsorption of X_{55} (X = Ni, Pd, and Pt) clusters is simulated on three different supports: (i) a three-layer model of MgO(100),

https://doi.org/10.1021/acs.jpcc.4c04213
J. Phys. Chem. C 2024, 128, 21331−21342

mimicking bulk MgO surfaces, referred to as MgO (3L); (ii) a MgO monolayer supported on Ag(100), labeled as MgO/Ag; and (iii) a model of a Ag-supported MgO monolayer, containing 25% oxygen trapped in hollow sites at the metal/oxide interface (MgO/O/Ag). The comparison between MgO (3L) and MgO/Ag is relevant to assess the different adsorptive properties of bulk MgO and metal−supported MgO thin films.

The interfacial oxygen significantly affects the work function and can promote the oxidation of adsorbates by allowing oxygen to permeate through the MgO film.[25] To verify this, we also studied models in which the oxygen atoms are bound to the X_{55} cluster (X/O/MgO/Ag). Finally, we complete this study by modeling the cluster behavior under oxidizing conditions, where it can be assumed that the oxygen loading on the system will exceed that of the oxygen atoms trapped at the MgO-Ag interface during growth (X/O_{exc}/MgO/Ag). The structures of the metal clusters and supports are depicted in Figure 1.

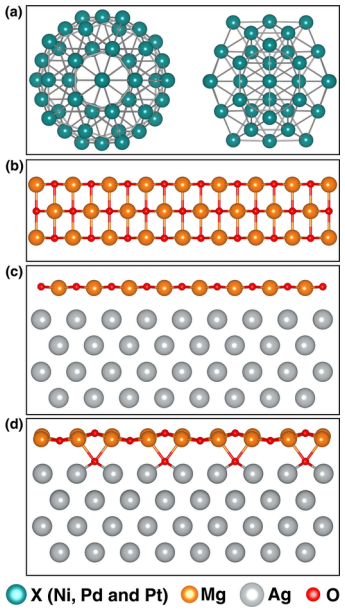

Figure 1. Schematic representation of (a) X_{55} clusters with ball-and-bond representation, (b) MgO (3L), (c) MgO/Ag, and (d) MgO/O/Ag supports.

Regarding the magnetic properties of the clusters, Ni_{55} demonstrates a total magnetization of 39.94 μ_B (0.73 μ_B per Ni atom), significantly higher than that of bulk Ni (0.55 μ_B per Ni atom).[67] Pd_{55} and Pt_{55} clusters, whose bulk metallic counterparts are nonmagnetic, exhibit smaller magnetic moments compared to Ni_{55}: 23.46 μ_B for Pd_{55}, 0.43 μ_B per Pd atom, and 11.21 μ_B for Pt_{55}, corresponding to 0.20 μ_B per Pt atom.

3.1. X_{55} Clusters on Free-Standing MgO. MgO (3L) is considered to be the first support to be investigated. The main structural, energetic, and magnetic properties of X_{55}/MgO(3L) are reported in Table 1. The side view of the relaxed investigated systems, along with the PDOS plots, are shown in Figure 2 and the corresponding top view of the structures, with calculated electrostatic potential graphs plotted along the z-axis, are illustrated in Figure S1 in the Supporting Information.[68]

All X_{55} clusters display negative values of E_{ads} on MgO (3L), indicating that their bonding to the substrate is stable at 0 K. The strength of the interaction follows the trend Pt_{55} (−11.70 eV) > Ni_{55} (−8.11 eV) > Pd_{55} (−7.74 eV). Upon adsorption, Ni_{55} acquires a negative charge ($\Delta\rho$) of −0.98 |e|. An even larger $\Delta\rho$ is transferred to Pd_{55} (−1.14 |e|) and Pt_{55} (−1.76 |e|). This is reflected in the large and positive interfacial dipole moment (D_e) established upon adsorption (Table 1). For Ni, only a slight decrease in the cluster magnetization (μ) is reported (from 39.94 μ_B to 37.65 μ_B, Table 1). The large residual magnetization is due, as expected, to the population of the orbitals of Ni atoms (Figure 2b). As illustrated in Figure 2b, it is worth mentioning that the metal states demonstrate notably elevated energy levels relative to the onset of the band of the O atoms, particularly in the case of Ni, compared to the case of Pd and Pt. The contribution to the total magnetization arising from the single Ni, Pd, Pt atoms has been checked, to conclude that there is no evidence of antiferromagnetic behavior, i.e. all atomic magnetic moments display the same sign. From a structural standpoint, it is important to mention that Ni_{55} and Pd_{55}, in the gas phase, display a perfect icosahedral structure, while Pt_{55} has a less regular shape. The analysis of the structural changes undergone upon adsorption on MgO(3L) is based on the descriptors reported in Table 1 (intermetallic distances and apical heights of the cluster with respect to the MgO surface). It results that Ni_{55} maintains its minimum, maximum, and average Ni−Ni distances almost unaltered upon adsorption on MgO(3L) (see Table 1). As illustrated in Figure 2a, six Ni−O bonds in the range of 1.9−2.1 Å are established at the interface with MgO. In the case of Pd_{55}, the formation of three Pd−O bonds (2.07−2.11 Å) at the interface is accompanied by a structural modification that results in the creation of several Pd−Pd intermetallic bonds, some as short as 2.5 Å, a distance not observed for gas-phase Pd_{55} (Table 1). For Pt_{55}, no significant perturbation of the closest Pt−Pt distances is observed when transitioning from gas-phase Pt_{55} to an adsorbed Pt_{55} cluster on MgO(3L) (see Table 1), while five Pt−O bonds are formed at distances between 2.13 and 2.18 Å. Finally, it should be noted that the apical metal atoms in Ni_{55} are positioned at a lower height relative to the apical MgO plane (9.37 Å) compared to Pd (10.83 Å) and Pt (10.38 Å), Table 1. This can be attributed to the smaller atomic radius of Ni, which belongs to the first transition series, in comparison to those of Pd and Pt.

3.2. From MgO(3L) to MgO/Ag: Impact of the Supporting Metal. Metal-supported oxide thin films display distinctive adsorptive properties compared with their bulk oxide counterparts. At first glance, for instance, one can observe from Figure 3a and Figure S2 (Supporting Information[68]) how the supported MgO monolayer tends to adopt a buckled configuration, with the O^{2-} ions protruding upward to bind the cluster, and the Mg^{2+} ions being pushed downward toward the Ag surface, contrasting with the rigidity exhibited by bulk MgO.

The first intriguing observation arises from a comparison of the E_{ads} of X_{55} clusters on MgO(3L) and MgO/Ag supports, as presented in Table 1. Notably, for Ni_{55}, a relatively modest increase in E_{ads} is observed (from −8.11 to −8.52 eV, representing a mere 7 meV increase per Ni atom). For Pd_{55}, a more substantial increase in E_{ads} is obtained (from −7.74 to −9.27 eV, 30 meV per Pd atom). In the case of the Pt_{55} cluster, the opposite trend is noted; the adsorption energy slightly decreases from −11.70 eV on MgO(3L) to −10.65 eV on MgO/Ag. One could analyze the main electronic and structural factors involved in this context.

An important factor to consider is that the electronic structure of MgO/Ag differs significantly from that of free-standing MgO. As shown in Figure 3b, a continuous manifold of Ag(100) states is present between the occupied and virtual bands of MgO, at

https://doi.org/10.1021/acs.jpcc.4c04213
J. Phys. Chem. C 2024, 128, 21331−21342

Table 1. Summary of Structural, Electronic, and Magnetic Features of X_{55} (X = Ni, Pd, and Pt) Clusters Interacting with MgO (3L) Support, MgO/Ag Support at 0 and 200 K, and MgO/O/Ag Support, and in the Presence of Oxygen Atoms Bound to the Clusters (X/O/MgO/Ag and X/O_{exc}/MgO/Ag)[a]

Structure	Top-Z (Å)	M-M'_{ave} (Å)	M-M'_{min} (Å)	M-M'_{max} (Å)	μ (μ_B)	$\Delta\rho$ (|e|)	D_e (|e| × Å)	$\Phi/\Delta\Phi$ (eV)	E_{ads} (eV)
Ni	–	2.35	2.29	2.40	39.94	–	–	4.52/0.00	–
Ni/MgO (3L)	9.37	2.34	2.26	2.42	37.65	−0.98	3.67	4.05/0.77	−8.11
Ni/MgO/Ag @ 0 K	9.41	2.34	2.22	2.42	38.70	−0.75	−0.02	4.19/0.01	−8.52
Ni/MgO/Ag @ 200 K	9.16	2.33	2.25	2.41	38.39	−0.28	−0.12	4.22/0.04	−10.28
Ni/MgO/O/Ag	9.47	2.35	2.28	2.42	39.20	1.47	0.52	4.34/0.18	−21.29
Ni/O/MgO/Ag	9.46	2.37	2.24	2.50	38.78	12.10	2.23	4.92/0.80	−42.21
Ni/O_{exc}/MgO/Ag	9.38	2.41	2.28	2.62	35.32	20.92	3.69	5.54/1.32	−73.75
Pd	–	2.66	2.60	2.69	23.46	–	–	4.47/0.00	–
Pd/MgO (3L)	10.83	2.65	2.51	2.72	20.16	−1.14	2.96	4.47/0.53	−7.74
Pd/MgO/Ag @ 0 K	10.75	2.64	2.42	2.73	17.20	−2.66	0.85	4.50/0.31	−9.27
Pd/MgO/Ag @ 200 K	10.08	2.61	2.53	2.69	7.96	−3.52	0.81	4.48/0.29	−11.51
Pd/MgO/O/Ag	10.75	2.64	2.45	2.72	17.46	−0.70	1.20	4.61/0.43	−18.15
Pd/O/MgO/Ag	10.79	2.65	2.45	2.78	−2.34	8.15	2.69	5.17/0.95	−26.22
Pd/O_{exc}/MgO/Ag	10.85	2.64	2.41	2.78	−1.05	12.20	3.55	5.50/1.27	−46.75
Pt	–	2.60	2.52	2.70	11.21	–	–	5.37/0.00	–
Pt/MgO (3L)	10.38	2.57	2.50	2.69	0.00	−1.76	4.49	5.00/0.84	−11.70
Pt/MgO/Ag @ 0 K	10.77	2.60	2.43	2.72	4.85	−3.62	2.20	4.97/0.78	−10.65
Pt/MgO/Ag @ 200 K	10.14	2.58	2.53	2.67	0.00	−4.71	2.39	4.99/0.79	−16.82
Pt/MgO/O/Ag	10.80	2.61	2.46	2.71	9.77	−1.32	2.72	5.20/0.97	−19.36
Pt/O/MgO/Ag	11.15	2.59	2.50	2.67	0.00	7.02	3.66	5.50/1.30	−25.67
Pt/O_{exc}/MgO/Ag	11.72	2.61	2.53	2.74	6.52	10.98	4.49	5.80/1.59	−46.69

[a]Height of the apical X atom with respect to the underlying surface (Top-Z); average (M-M'_{ave}), minimum (M-M'_{min}), and maximum (M-M'_{max}) first-neighbor metal−metal distances; total magnetization in the X_{55} cluster (μ); total transferred charge of X_{55} ($\Delta\rho$); interfacial dipole moment (D_e); work function (Φ); work function variation with respect to the clean surface ($\Delta\phi$); and adsorption energy (E_{ads}).

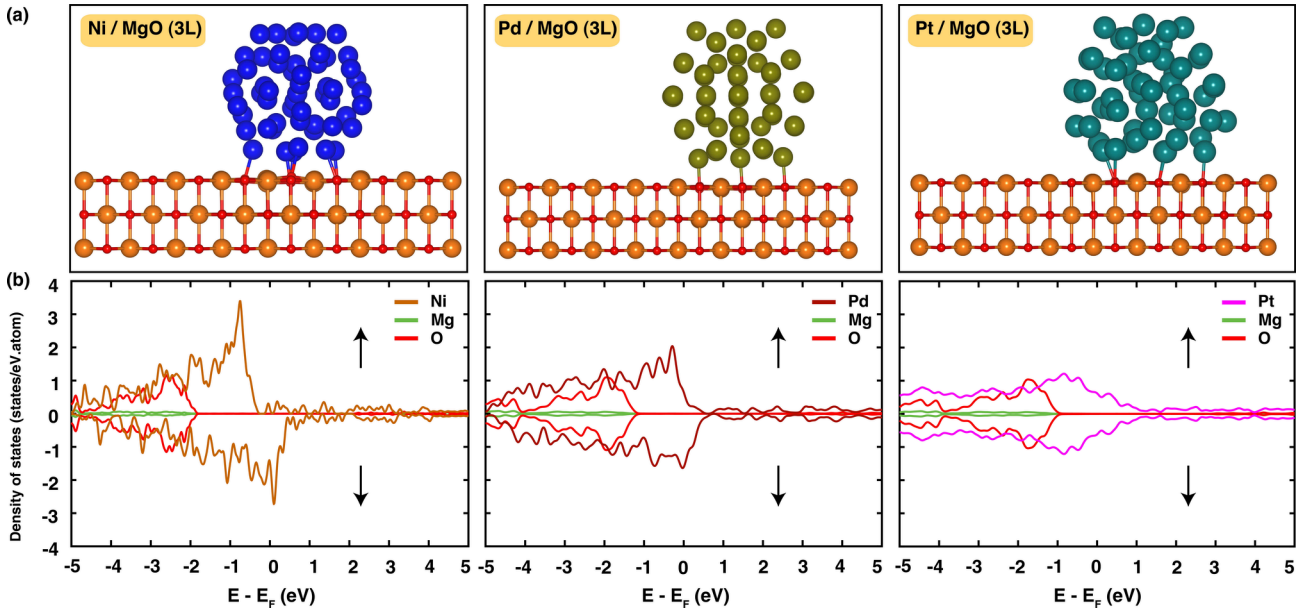

Figure 2. (a) Side views of optimized structures of Ni_{55}, Pd_{55}, and Pt_{55} clusters on a MgO (3L) support, and (b) normalized projected density of states (PDOS) of the corresponding structures.

energies overlapping those of the bands of the X_{55} clusters. This allows for a direct process of charge injection or depletion from the orbitals of an adsorbate directly to the underlying Ag support via tunneling through the MgO thin layer.[69] In the case of Ni_{55}, for instance, the surface-to-cluster charge donation observed in MgO (3L) (−0.98 |e|) is partially compensated by a back-donation from the cluster toward the support. Consequently, the resulting $\Delta\rho$ remains negative (−0.75 |e|) but is smaller compared to that in MgO (3L). The resulting D_e is negligible due to the compensation between opposite components: the positive dipole at the MgO/Ni_{55} interface and the negative dipole at the MgO/Ag interface. The μ value of Ni_{55} is 38.70 μ_B, an intermediate value between that of the gas-phase cluster and Ni_{55}/MgO(3L). The Ni atoms closer to the MgO film display a

https://doi.org/10.1021/acs.jpcc.4c04213
J. Phys. Chem. C 2024, 128, 21331−21342

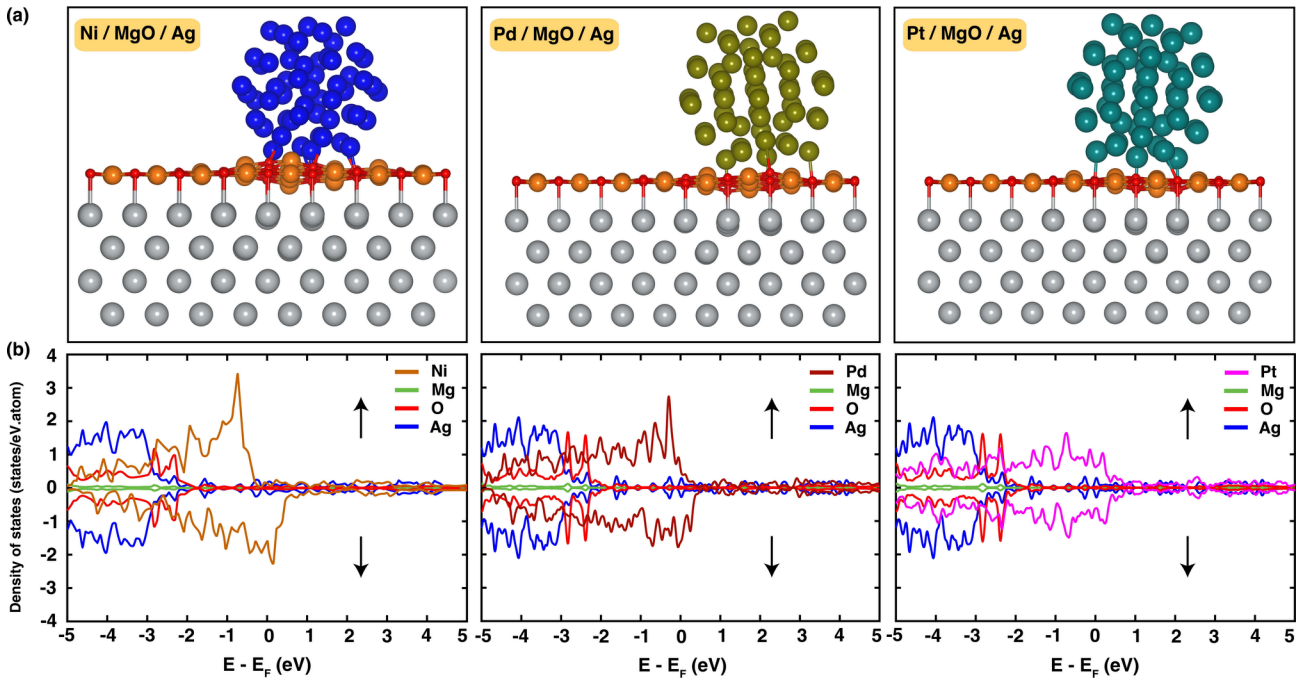

Figure 3. (a) Side views of optimized structures of X_{55} clusters on a MgO/Ag support (X_{55}/MgO/Ag), and (b) normalized PDOS of Ni_{55}/MgO/Ag (left), Pd_{55}/MgO/Ag (middle), and Pt_{55}/MgO/Ag (right).

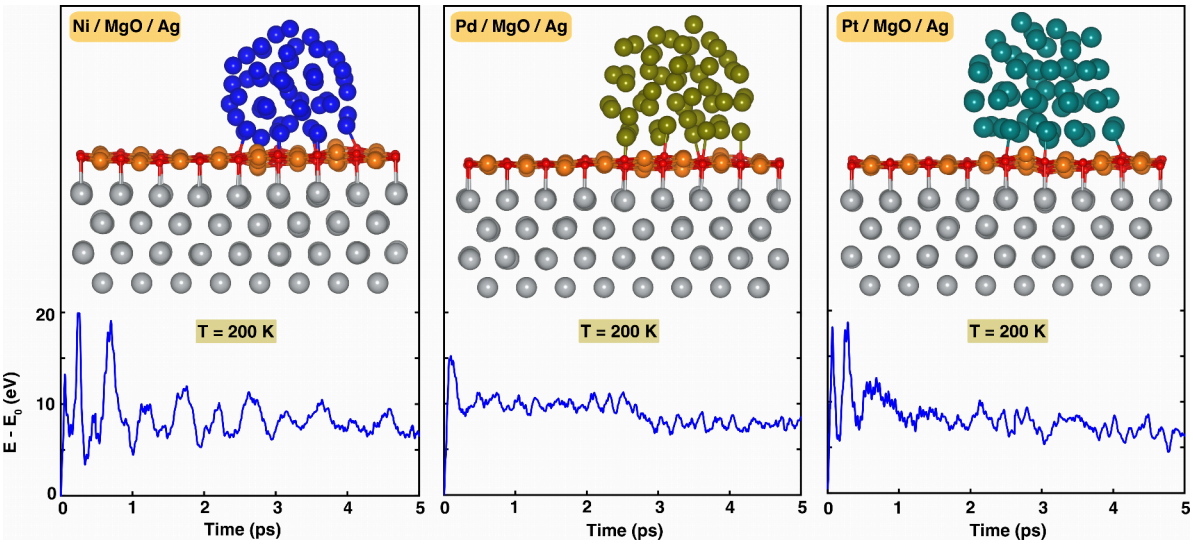

Figure 4. Variations in the gradient values of the total energies for the X_{55}/MgO/Ag structures as a function of simulation time at T = 200 K. The insets show the final atomic arrangements captured at the end of the simulation. E_0 and E denote the total energies of the systems at 0 and 200 K, respectively.

smaller magnetization, in general, as highlighted in Figure S3 (Supporting Information[68]).

A small increase in Φ (0.18 eV) with respect to bare MgO/Ag is reported. The main structural features of Ni_{55}/MgO/Ag closely resemble those of Ni_{55}/MgO(3L), as shown in Table 1. For Pd_{55}/MgO/Ag, the charge injected from the support into the cluster is more than double that on MgO(3L), with $\Delta\rho$ = −2.66 |e|. This induces a further decrease in Pd_{55} magnetization to 17.20 μ_B, as shown in Table 1. The D_e in the cell is still positive (0.85 |e| × Å), but it is smaller compared to that of Pd_{55}/MgO(3L). The increase in work function with respect to the bare substrate is larger ($\Delta\Phi$ = +0.31 eV) compared with the case of Ni. The structural alteration of Pd_{55} induces new intermetallic bonds at an even shorter distance of 2.42 Å, as shown in Table 1.

For Pt_{55}/MgO/Ag, similar to what has been reported for Pd, the charge transfer is almost double in the case of MgO/Ag ($\Delta\rho$ = −3.62 |e|) compared to MgO(3L) ($\Delta\rho$ = −1.76 |e|). The values of D_e, Φ, and $\Delta\Phi$ also display the highest magnitudes observed within the series on MgO/Ag. Interestingly, the Pt_{55} cluster appears to be slightly elongated on Ag-supported MgO, as evidenced by the larger Top-Z value of 10.77 Å. Some Pt−Pt distances closer to 2.40 Å appear, indicating further evidence of significant structural distortion.

We further checked the reliability of the adopted approach by performing some supplemental structural relaxations based on the optimized structures described above. Namely, the structure obtained for Ni_{55}/MgO/Ag was used as an initial guess for Pd_{55}/MgO/Ag and Pt_{55}/MgO/Ag. An analogous procedure was

https://doi.org/10.1021/acs.jpcc.4c04213
J. Phys. Chem. C 2024, 128, 21331−21342

adopted in the cases of Pd and Pt. Given the remarkably smaller atomic radius of Ni compared to Pd and Pt, Ni_{55}/MgO/Ag is a poor guess structure for larger metals, leading to nonconverged calculations. Any attempt to relax Ni_{55}/MgO/Ag starting from structures obtained for Pd and Pt led to structures highly destabilized in energy. Vice versa, Pd and Pt are more suitable for interchange, but these further tests did not lead to structures more stable than those described above.

The stability of the X_{55}/MgO/Ag structures at a temperature of 200 K, mimicking the growth and annealing processes of metallic aggregates on such substrates, has been thoroughly examined through AIMD calculations spanning on a trajectory of 5 ps, as depicted in Figure 4. The top panel of the figure provides side views of the examined systems, revealing that the supported X_{55} clusters exhibit no discernible structural reorganization or disintegration at T = 200 K. A static relaxation starting from the structures in Figure 4 was performed, and it resulted that, in all cases, more stable structures are obtained with respect to those statically relaxed at 0 K. The energy gain is quite small in the case of Ni (0.03 eV/atom) and Pd (0.04 eV/atom) but remarkable in the case of Pt (0.11 eV/atom). A detailed structural analysis reveals that, in the case of Ni_{55}, no major structural changes are induced in the cluster after the annealing at 200 K, besides a remarkable decrease in the apical height from 9.41 to 9.16 Å, Table 1. The same decrease in height is reported for Pd_{55} and Pt_{55} annealed at 200 K, along with an increase in the M-M'_{min} distance. It is also worth mentioning that the number of X-O bonds at the cluster/MgO interface increases after annealing from 8 to 12 (Ni), 4 to 7 (Pd), and 4 to 5 (Pt). This suggests that the clusters increase their interaction area to MgO as an effect of the thermal annealing. No major changes are reported for Φ and D_e. The negative charge of Pd_{55} and Pt_{55} slightly increases after the annealing at 200 K. This observation underscores the robustness of the structures under investigation, suggesting that they maintain their integrity and even strengthen their adhesion to the support under the influence of a typical annealing temperature. Furthermore, the bottom panel of Figure 4 illustrates the oscillating behavior of the thermal energy gradient, $E - E_0$. The absence of significant deviations or abrupt changes in this energy gradient further supports the conclusion that there are no notable structural alterations or phase transitions occurring within the examined systems at the specified temperature. This stabilization under thermal conditions highlights the potential suitability of these structures for catalytic studies of model systems. It must be stated that the temperature adopted in the AIMD simulations is realistic with respect to typical deposition protocols of metallic particles on supported oxide thin films, as is done in studies on model catalytic systems. A working catalyst, in contrast, is often exposed to higher temperatures, which could eventually challenge the actual stability of the supported nanoparticles. The time span of the AIMD simulations is limited by the relatively high cost of these calculations.

3.3. Oxidation of X_{55} Clusters on MgO/Ag: Role of Interfacial Oxygen and Exposure to Oxidizing Environments. The oxidation of metallic nanoclusters greatly affects their stability and adhesion to the substrate as well as their electronic, magnetic, and chemical properties. As previously demonstrated for smaller Ni_{4-6} aggregates,[25] clusters deposited on MgO monolayers that are reactively grown on Ag undergo spontaneous oxidation. This is attributed to the substantial amount of oxygen trapped at the MgO-Ag interface, which has the potential to diffuse and oxidize the adsorbates. Thus, we compare the adsorption of X_{55} clusters on a MgO/Ag substrate with a 25% excess of oxygen at the interface (16 O atoms per cell) to the previously discussed scenario where the MgO/Ag interface is sharp, exposing a clean Ag(100) surface to a perfectly stoichiometric MgO monolayer. Next, we assess the stability of this X/MgO/O/Ag structures against the case where an equivalent number of oxygen (16 O atoms per cell) atoms is directly bonded to the metal cluster, namely X/O/MgO/Ag, via a reverse spillover process from the MgO/Ag interface to the adsorbed clusters. The behavior of the supported X_{55} clusters under oxidative conditions is further tested by adding 32 more oxygen atoms per cell, thus simulating the exposure of the supported nanocluster to an oxidizing reaction environment (X/O_{exc}/MgO/Ag). A thorough exploration of all possible adsorption sites and the distribution of the oxygen atoms on the nanoparticles would be demanding. Therefore, the structures analyzed in this Section were built based on chemical intuition and are not based on an exhaustive exploration of all possible minima, which may slightly affect the final results. The whole process is depicted schematically in Figure 5.

For Ni_{55}, we observe a significant increase in E_{ads} on MgO/O/Ag (−21.29 eV) compared with the MgO/Ag monolayer without interfacial oxygen (−8.52 eV). The crystal structure of Ni_{55}/MgO/O/Ag is depicted in Figure 6a. Interestingly, this significant enhancement in energetic stability coincides with a reverse charge transfer, wherein, contrary to previous cases, the Ni cluster now bears a positive charge ($\Delta\rho$ = +1.47 |e|, Table 1). The shift of the Ni(3d) band edge above the Fermi level is evident from the PDOS plot in Figure 6b. This is due to the larger Φ of MgO/O/Ag (4.65 eV) compared to MgO/Ag (4.30 eV), which is associated with the oxidation of Ag in the presence of interfacial oxygen, as previously reported.[23] Despite the change in the ionization of Ni_{55}, the magnetization of the cluster remains similar to that of the previous case (μ = 39.20 μ_B). From a structural point of view, no major deviations in the Ni−Ni bond distances are noted. The scenario changes further when considering the possibility of oxygen reverse spillover from the MgO to the Ni cluster, involving a hypothetical concerted mechanism in which oxygen vacancies in MgO are refilled by oxygen atoms segregated at the MgO/Ag interface. Passing from Ni_{55}/MgO/O/Ag to Ni_{55}/O/MgO/Ag, as seen in Figure 6a and c, respectively, the cluster experiences stronger energetic stabilization (E_{ads} = −42.21 eV), with its positive charge increasing to 12.10 |e|.

The reverse spillover is accompanied by a large positive D_e (+2.23 |e| × Å), along with changes in the M-M'_{max}, attributed to the strong bonding of oxygen atoms at the cluster periphery, as illustrated in Figure 6c.

For Pd_{55}, a notable increase in the E_{ads} of the cluster is seen compared to the support lacking interfacial oxygen (−18.15 eV, Table 1). However, at variance with the calculated value for Ni, its charge remains negative ($\Delta\rho$ = −0.70 |e|), though it is smaller than that obtained for MgO/Ag. No major changes in the μ, Φ, D_e, and Pd−Pd distances within the cluster are observed compared to those of MgO/Ag. The reverse oxygen spillover from the MgO/Ag interface to the cluster is highly favorable, as indicated by the increase in E_{ads} to −26.22 eV (Table 1). The Φ of the system (Pd_{55}/O/MgO/Ag) also increases remarkably by up to 0.95 eV compared to bare silver. The oxidation of Pd_{55} due to reverse oxygen spillover is evident by the reversal of the sign in the charge ($\Delta\rho$ = +8.15 |e|), and is also noticeable from the PDOS plot in Figure 6d. Alongside a substantial reduction in the net magnetization of the cluster (μ = −2.34 μ_B), an increase in

https://doi.org/10.1021/acs.jpcc.4c04213
J. Phys. Chem. C 2024, 128, 21331−21342

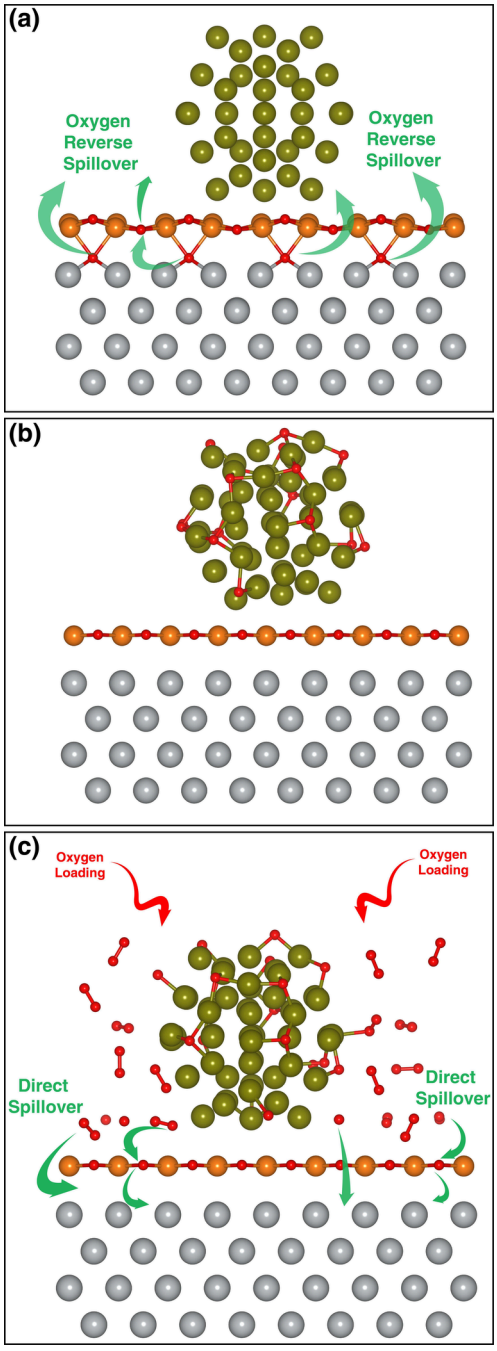

Figure 5. Schematic representation of (a) X/MgO/O/Ag, (b) X/O/MgO/Ag, and (c) X/O_{exc}/MgO/Ag structures. The processes of oxygen reverse spillover and direct spillover are illustrated.

the D_e and Φ values is noticed. The M-M'_{min}, M-M'_{ave}, and M-M'_{max} distances between Pd−Pd first neighbors do not change dramatically, aside from a slight increase in M-M'_{max}, suggesting that the Pd_{55} surface can accommodate a considerable number of adsorbed oxygen atoms without undergoing drastic structural rearrangements. Under certain aspects, the case of Pt_{55} closely resembles that of Pd_{55}. For instance, an increase in the adsorption energy (E_{ads} = −19.36 eV) and a notable decrease in the negative charge on the cluster ($\Delta\rho$ = −1.32 |e|) are observed compared to MgO/Ag, while the Pt−Pt distances remain largely unchanged, as shown in Table 1. However, unlike Ni_{55} and Pd_{55}, the Pt_{55} cluster experiences a notable increase in magnetization in the presence of interfacial oxygen on MgO/O/Ag (μ = 9.77 μ_B). Additionally, D_e and Φ also increase. Upon reverse oxygen spillover, considerable stabilization is observed as the E_{ads} transitions from −19.36 eV (Pt/MgO/O/Ag) to −25.67 eV (Pt/O/MgO/Ag). The depletion of the occupied Pt states is visible in Figure 6 d, and the charge of the Pt_{55} cluster is now positive, + 7.02 |e|. A sizable increase in the D_e and Φ is also calculated, and the results are presented in Table 1. No significant changes in the Pt−Pt distances are observed. A trend emerges comparing the PDOS plots in Figures 3, b and d, where, in the case of Ni clusters, the density of states at the Fermi level is large, and mostly due to the contributions from Ni orbitals. Furthermore, Figures S4 and S5 in the Supporting Information[68] depict the top views of the relaxed structures of X_{55}/MgO/O/Ag and X_{55}/O/MgO/Ag systems, respectively, along with the electrostatic potential of these structures. The magnetization of the metallic adducts can also be appreciated. In comparison, adsorbed Pd_{55} and Pt_{55} particles display a smaller density of states close to the Fermi level, and a much smaller residual magnetization.

Thus, one can observe how the presence of oxygen trapped at the interface will result in covering the surface of the supported metal nanoparticles with oxygen. The thermodynamic gain associated with this process is supported by the discussed data. This is an important finding that highlights the interest of group-10 clusters on MgO-Ag for studies on model catalysts. However, it would be intriguing to investigate how these partially oxidized clusters behave when exposed to an oxidizing atmosphere in a hypothetical reactive environment. We modeled this by adding 32 additional oxygen atoms to the cluster surface and then performing a structural relaxation. These cases are labeled as X/O_{exc}/MgO/Ag (with X = Ni, Pd, and Pt) in Table 1, and the side views of relaxed structures and PDOS plots are displayed in Figure 7a and b, respectively. Additionally, the top views of ground state structures and the electrostatic potential of the corresponding systems are illustrated in Figure S6 in the Supporting Information.[68] An intriguing observation is apparent in Figure 7a: despite the initial placement of additional oxygen atoms on the supported clusters and the surface of the MgO monolayer, following the relaxation process, various types of oxygen species are present: (i) O adsorbed on X_{55}, (ii) molecular O_2 species, and (iii) the MgO/Ag interface once again bears a remarkable concentration of oxygen atoms. More precisely, a migration path is observed in which specific oxygen atoms diffuse from the cluster and the top surface of the MgO monolayer to the MgO lattice sites, subsequently displacing the lattice oxygen atoms downward at the MgO/Ag interface. At the end of the relaxation, the interface contains 16 O atoms for Ni_{55}, 23 O atoms for Pd_{55} and 21 O atoms for Pt_{55}. This indicates that the MgO/Ag interface can function as a buffer, exhibiting either reverse oxygen spillover toward the X_{55} clusters under oxygen-poor conditions or direct oxygen spillover under oxygen-rich conditions. For all three metal clusters, the adsorption energy, E_{ads}, was computed relative to those of MgO/O/Ag and 16 molecules of O_2 in the gas phase. It is observed that E_{ads} becomes more negative, indicating that oxidation of the system can spontaneously occur, as the net charge of the supported nanoparticles becomes more positive. This is particularly evident for Ni, where E_{ads} is now −73.75 eV and the $\Delta\rho$ of Ni_{55} is +20.92 |e|. Additionally, the μ value of the system decreases further to 35.32 μ_B. As anticipated under oxidizing conditions, both the D_e and Φ increase (Table 1). The average Ni−Ni first-neighbor distance (Ni − Ni_{ave} = 2.21 Å) and the

https://doi.org/10.1021/acs.jpcc.4c04213
J. Phys. Chem. C 2024, 128, 21331−21342

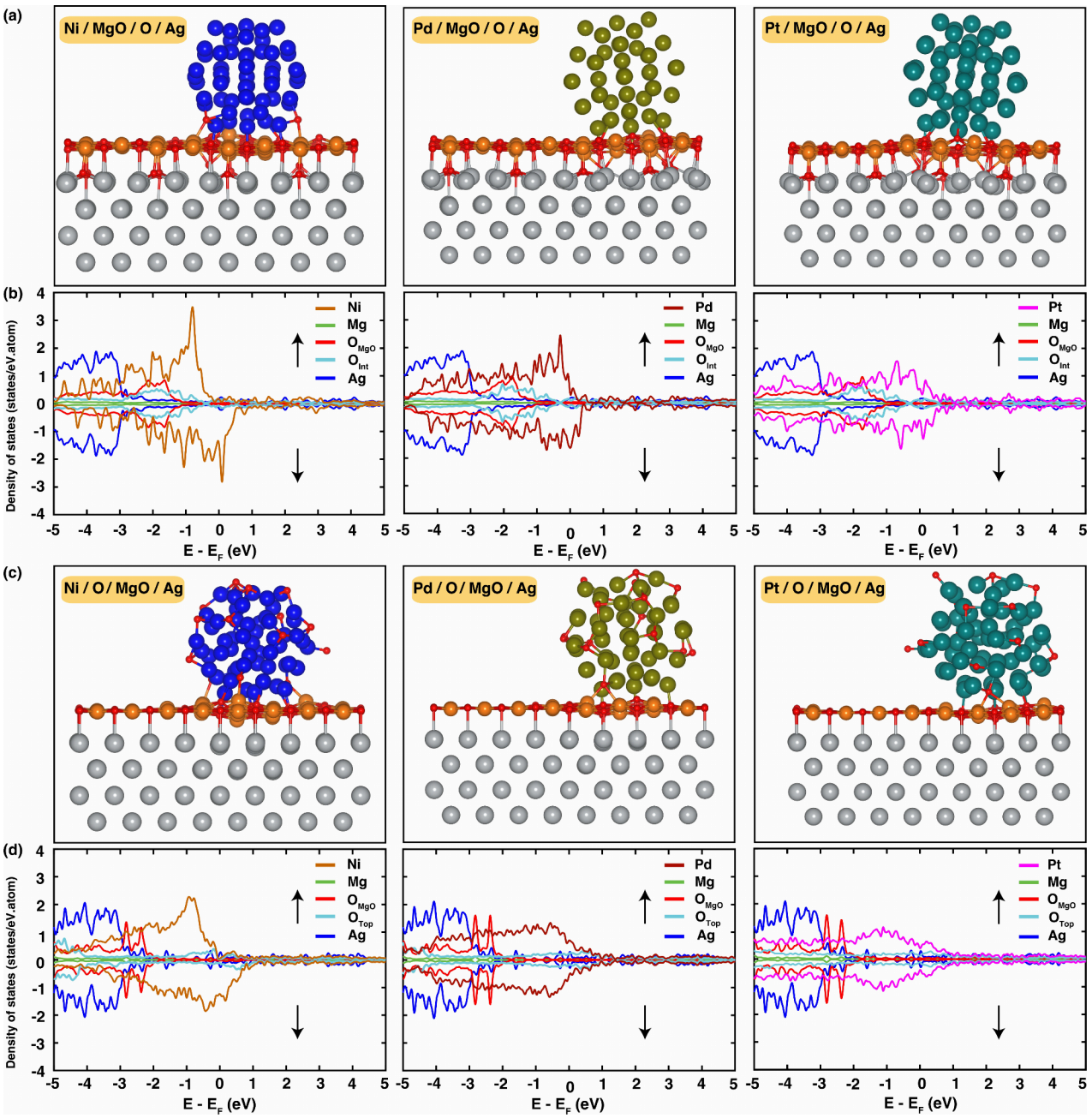

Figure 6. (a) Side views of optimized structures of Ni_{55}, Pd_{55}, and Pt_{55} nanoclusters on a MgO/Ag support with oxygen at the interface, (b) PDOS of the corresponding structures, (c) Side views of the atomic configurations of relaxed X_{55} clusters on a MgO/Ag support in the presence of low-dosage oxygen (X_{55}/O/MgO/Ag), and (d) calculated PDOS of Ni_{55}/O/MgO/Ag (left), Pd_{55}/O/MgO/Ag (middle), and Pt_{55}/O/MgO/Ag (right).

maximum Ni−Ni first-neighbor distance (Ni − Ni_{max} = 2.62 Å) are notably larger compared to gas-phase Ni_{55}. This indicates that at high oxygen loading certain Ni atoms at the periphery of the nanoparticle lose contact, initiating the formation of a nickel oxide layer. Likewise, a higher amount of oxygen can be stabilized on Pd_{55}, with E_{ads} = −46.75 eV (Table 1). The charge lost by the cluster ($\Delta\rho$ = 12.20 |e|) increases with oxygen loading but remains significantly smaller compared to the case of Ni. The μ further decreases to −1.05 μ_B. Additionally, a significant increase in D_e and Φ ($\Delta\Phi$ = +1.27 eV relative to bare Ag) is acquired. Notably, unlike Ni, there is a slight reduction in both the average and minimum Pd−Pd distances, as indicated in Table 1. In the case of Pt_{55} as well, the system can accommodate a larger quantity of oxygen in terms of thermodynamic stability (E_{ads} = −46.69 eV, Table 1). An increase in the positive charge on the cluster (10.98 |e|) is observed. Moreover, a small residual μ is present on the oxidized Pt nanoparticles, while both Φ and D_e increase (see Table 1). Similarly to Pd, no significant increase in the metal−metal first-neighbor bonding distances is observed. The main findings revealed so far concern the remarkable structural stability demonstrated by these supported metallic particles, even under realistic conditions for deposition and annealing. The magnetic properties of the supported clusters are influenced by the support through interfacial charge transfer phenomena, which are regulated by the surface's work function. In this context, the role of interfacial oxygen is significant, as it promotes the withdrawal of electron charge from X_{55} clusters, thereby enhancing their adsorption. Furthermore, the X_{55}

https://doi.org/10.1021/acs.jpcc.4c04213
J. Phys. Chem. C 2024, 128, 21331−21342

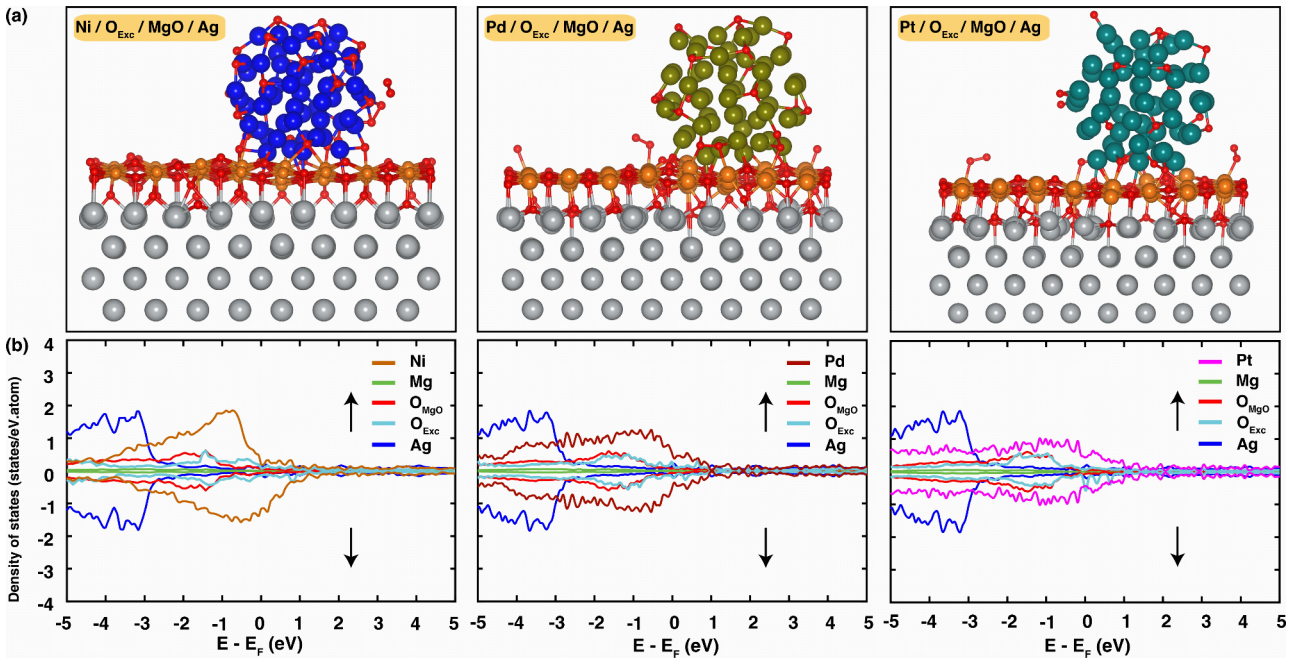

Figure 7. (a) Views of optimized structures of Ni_{55}, Pd_{55}, and Pt_{55} nanoclusters on a MgO/Ag support in the presence of high-dosage oxygen, and (b) PDOS of Ni_{55}/O_{exc}/MgO/Ag (left), Pd_{55}/O_{exc}/MgO/Ag (middle), and Pt_{55}/O_{exc}/MgO/Ag (right).

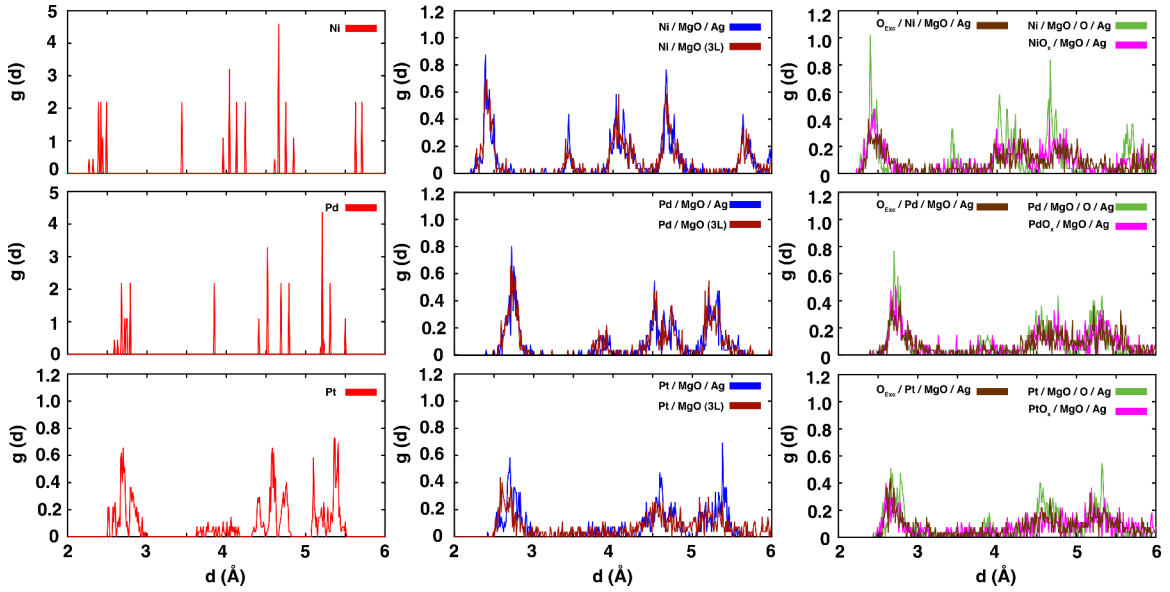

Figure 8. Graphs of radial distribution functions [g(r)] with respect to the distance distribution (d) between metal atoms within the clusters for both gas-phase clusters and supported clusters.

clusters are likely to be partially covered by oxygen atoms diffusing from the metal-oxide interface to the cluster surface. Under oxidizing conditions, the reverse process occurs, and the oxygen loading on the metal particles is self-regulated by the spontaneous migration to the metal-oxide interface. When oxygen species are adsorbed on their surfaces, X_{55} clusters display structural modifications. Further analysis of the metal−metal bonding distance distribution is provided in the next section.

3.4. Radial Distribution Function of X_{55} Nanoclusters on Examined Supports. The radial distribution function (RDF) is a measure that describes how the particle density varies as a function of distance from a reference particle within a system. For nanoclusters, which are small aggregates of atoms, the RDF offers insights into the spatial arrangement and structural order within the cluster. By calculating and analyzing the RDF plot, one can infer the degree of crystallinity and the presence of disorder in the nanocluster's structure. Here, we obtained the RDF for gas-phase and adsorbed X_{55} (X = Ni, Pd, and Pt) clusters on the studied supports and the results are illustrated in Figure 8. Ni_{55} and Pd_{55} clusters maintain an icosahedral regular shape in the gas phase, as evidenced by the sharp peaks observed in the plot. The first peaks, corresponding to the distance distribution between first neighbors, occur at slightly shorter distances compared to the bulk (2.46 and 2.75 Å, respectively). These characteristics can be attributed to the

https://doi.org/10.1021/acs.jpcc.4c04213
J. Phys. Chem. C 2024, 128, 21331−21342

relaxation of atoms at the surface of the cluster. It clearly appears that Pd follows the same peak distribution of Ni, only shifted at larger distances, as expected. Pt_{55}, on the contrary, exhibits a more disordered structure, consistent with previous theoretical findings.[66] The deposition of X_{55} on the surface of MgO(3L) or MgO/Ag induces some structural changes in the interfacial zone of the X_{55} clusters, as evidenced by the broadening of the peaks in the RDF. It is intriguing that on MgO/Ag, the peaks appear taller and slightly sharper compared to MgO(3L) for all the studied nanoclusters. This suggests a more pronounced tendency of the X_{55} clusters to adapt to the surface structure on bulk MgO compared to that on MgO thin films. This phenomenon may be attributed to the enhanced flexibility of the MgO monolayer supported on Ag compared to its free-standing counterpart. Indeed, upon comparison of Figures 2 and 3, it becomes apparent that the MgO monolayer in MgO/Ag is distorted upon contact with the adsorbed X_{55} particles, whereas no visible distortion is exhibited by the topmost layer of MgO(3L). In the latter case, the X_{55} clusters experience greater distortion when wet the surface. The adsorption of oxygen species on the clusters (right column of Figure 8) induces additional disorder in the clusters, as demonstrated by the decrease in peak height and further broadening across a wide range of interatomic distances. The spreading of the Ni−Ni distances as the oxygen loading increases (Ni/O_{exc}/MgO/Ag), indicative of a greater degree of structural disorder, is evident in the RDF plots. A similar trend is observed for Pd and Pt.

4. CONCLUSIONS

In conclusion, we investigate the adsorption of X_{55} (X=Ni, Pd, and Pt) clusters on free-standing MgO and a MgO monolayer supported on Ag, in both the absence and presence of oxygen. The most significant finding is that oxygen spillover can occur bidirectionally: from MgO/Ag to the adsorbed clusters (in oxygen-poor atmosphere) or vice versa (under oxygen-rich atmosphere), for all metals studied here. The metal/oxide interface may thus function as a buffer, regulating the oxidation and reduction processes encountered by the supported nanoparticles when exposed to the atmosphere, thereby augmenting their stability. This fact bears direct and significant implications for catalytic studies using model systems. Additionally, it is noteworthy that all X_{55} clusters on MgO/Ag exhibit stability up to 200 K. Analysis of the data set by metal or type of support reveals a complex yet intriguing scenario. In general, Ni exhibits the highest tolerance among group-10 metals under oxidizing conditions and is more prone to donating charge to adsorbed oxygen species. Ni displays larger residual magnetization on each support compared to that of Pd and Pt. The trends in E_{ads} are more complex to delineate. On MgO(3L), they follow the order Pt > Ni > Pd, and on MgO/Ag, we observe Pt > Pd > Ni. In both cases, all clusters are negatively charged, and the E_{ads} is likely influenced by structural factors such as metal−oxygen matching at the interface. When oxygen is involved, either as an interfacial species or in direct contact with the X_{55} clusters, a clear trend emerges: Ni > Pd ≈ Pt. From a structural standpoint, Ni and Pd begin with highly symmetric icosahedral structures (Pt is more disordered), which are well preserved, especially on MgO monolayers that are more flexible and tend to conform to metallic particles. The adsorption of oxygen species on the particles induces an increase in structural disorder, as clearly evidenced by the radial distribution function (RDF) plots and the metal−metal distances, particularly in the case of Ni. Our results provide a comprehensive overview of the adsorption process of X_{55} nanoclusters on different supports and efficiently present a wide range of scenarios, which can subsequently be utilized as models for experimental studies.

■ ASSOCIATED CONTENT

Supporting Information

The Supporting Information is available free of charge at https://pubs.acs.org/doi/10.1021/acs.jpcc.4c04213.

Top views and planar averages of the electrostatic potential along the z-direction for optimized structures of X_{55} (X = Ni, Pd, and Pt) clusters on various supports: MgO (3L), MgO/Ag, MgO/Ag with oxygen at the interface, MgO/Ag with low-dosage oxygen, and MgO/Ag with high-dosage oxygen and magnetization of Ni atoms vs z-coordinate for MgO/Ag and MgO/O/Ag supports (PDF)

■ AUTHOR INFORMATION

Corresponding Authors

Mirali Jahangirzadeh Varjovi − *Department of Materials Science, University of Milano-Bicocca, 20125 Milano, Italy;* orcid.org/0000-0002-7700-9973; Email: mirali.jahangirzadeh@gmail.com

Sergio Tosoni − *Department of Materials Science, University of Milano-Bicocca, 20125 Milano, Italy; Department of Materials Science, University of Milano-Bicocca, 20125 Milano, Italy;* orcid.org/0000-0001-5700-4086; Email: sergio.tosoni@unimib.it

Complete contact information is available at: https://pubs.acs.org/10.1021/acs.jpcc.4c04213

Notes

The authors declare no competing financial interest.

■ ACKNOWLEDGMENTS

We gratefully acknowledge financial support from the European Union-Next Generation EU and the Italian Ministry of the University (MUR) through the PRIN projects 2022LS74H2 SUMCAR and P20227XSAH BiNano. We acknowledge the CINECA award under the ISCRA initiative, for the availability of high-performance computing resources and support. M.J.V. specifically acknowledges the utilization of EuroHPC resources at the CINECA Supercomputing Centre in Italy (through Project No. EHPC-BEN-2023B09-015 and EHPC-BEN-2024B03-052).

■ REFERENCES

(1) Monai, M.; Gambino, M.; Wannakao, S.; Weckhuysen, B. M. Propane to olefins tandem catalysis: a selective route towards light olefins production. *Chem. Soc. Rev.* **2021**, *50*, 11503−11529.

(2) Chorkendorff, I.; Niemantsverdriet, J. *Concepts of Modern Catalysis and Kinetics*, 3rd ed.; Wiley-VCH: Germany, 2017.

(3) Xia, Y.; Yang, H.; Campbell, C. T. Nanoparticles for catalysis. *Acc. Chem. Res.* **2013**, *46*, 1671−1672.

(4) Astruc, D. Introduction: Nanoparticles in Catalysis. *Chem. Rev.* **2020**, *120*, 461−463.

(5) Ma, Z.; Zaera, F.; Roe, T., Vickery, J. In *Encycl. Inorg. Chem.*, Eds.; John Wiley & Sons, Ltd: Chichester, UK, 2006; Vol. *30*; pp 27−38.

(6) Tauster, S. Strong metal-support interactions. *Acc. Chem. Res.* **1987**, *20*, 389−394.

(7) Dulub, O.; Hebenstreit, W.; Diebold, U. Imaging cluster surfaces with atomic resolution: the strong metal-support interaction state of Pt supported on TiO 2 (110). *Phys. Rev. Lett.* **2000**, *84*, 3646.

(8) Qin, Z.-H.; Lewandowski, M.; Sun, Y.-N.; Shaikhutdinov, S.; Freund, H.-J. Morphology and CO adsorption on platinum supported on thin Fe3O4 (111) films. *J. Condens. Matter Phys.* **2009**, *21*, 134019.
(9) Lewandowski, M.; Sun, Y.-N.; Qin, Z.-H.; Shaikhutdinov, S.; Freund, H.-J. Promotional effect of metal encapsulation on reactivity of iron oxide supported Pt catalysts. *Appl. Catal.* **2011**, *391*, 407−410.
(10) Park, J. Y.; Baker, L. R.; Somorjai, G. A. Role of hot electrons and metal−oxide interfaces in surface chemistry and catalytic reactions. *Chem. Rev.* **2015**, *115*, 2781−2817.
(11) Lunkenbein, T.; Schumann, J.; Behrens, M.; Schlögl, R.; Willinger, M. G. Formation of a ZnO overlayer in industrial Cu/ZnO/Al2O3 catalysts induced by strong metal−support interactions. *Angew. Chem.* **2015**, *127*, 4627−4631.
(12) Polo-Garzon, F.; Blum, T. F.; Bao, Z.; Wang, K.; Fung, V.; Huang, Z.; Bickel, E. E.; Jiang, D.-e.; Chi, M.; Wu, Z. In situ strong metal−support interaction (SMSI) affects catalytic alcohol conversion. *ACS Catal.* **2021**, *11*, 1938−1945.
(13) Liu, L.; Corma, A. Metal catalysts for heterogeneous catalysis: from single atoms to nanoclusters and nanoparticles. *Chem. Rev.* **2018**, *118*, 4981−5079.
(14) Valden, M.; Lai, X.; Goodman, D. Onset of catalytic activity of gold clusters on titania with the appearance of nonmetallic properties. *Science* **1998**, *281*, 1647−1650.
(15) Bus, E.; Prins, R.; van Bokhoven, J. A. Origin of the cluster-size effect in the hydrogenation of cinnamaldehyde over supported Au catalysts. *Catal. Commun.* **2007**, *8*, 1397−1402.
(16) Ruiz Puigdollers, A.; Schlexer, P.; Tosoni, S.; Pacchioni, G. Increasing oxide reducibility: the role of metal/oxide interfaces in the formation of oxygen vacancies. *ACS Catal.* **2017**, *7*, 6493−6513.
(17) Zambelli, T.; Wintterlin, J.; Trost, J.; Ertl, G. Identification of the" active sites" of a surface-catalyzed reaction. *Science* **1996**, *273*, 1688−1690.
(18) Nilius, N. Properties of oxide thin films and their adsorption behavior studied by scanning tunneling microscopy and conductance spectroscopy. *Surf. Sci. Rep.* **2009**, *64*, 595−659.
(19) Giordano, L.; Pacchioni, G. Oxide films at the nanoscale: new structures, new functions, and new materials. *Acc. Chem. Res.* **2011**, *44*, 1244−1252.
(20) Pacchioni, G.; Freund, H. Electron transfer at oxide surfaces. The MgO paradigm: from defects to ultrathin films. *Chem. Rev.* **2013**, *113*, 4035−4072.
(21) Ricci, D.; Bongiorno, A.; Pacchioni, G.; Landman, U. others Bonding trends and dimensionality crossover of gold nanoclusters on metal-supported MgO thin films. *Phys. Rev. Lett.* **2006**, *97*, 036106.
(22) Calaza, F.; Stiehler, C.; Fujimori, Y.; Sterrer, M.; Beeg, S.; Ruiz-Oses, M.; Nilius, N.; Heyde, M.; Parviainen, T.; Honkala, K.; et al. others Carbon dioxide activation and reaction induced by electron transfer at an oxide−metal interface. *Angew. Chem., Int. Ed.* **2015**, *54*, 12484−12487.
(23) Pal, J.; Smerieri, M.; Celasco, E.; Savio, L.; Vattuone, L.; Ferrando, R.; Tosoni, S.; Giordano, L.; Pacchioni, G.; Rocca, M. How growing conditions and interfacial oxygen affect the final morphology of MgO/Ag (100) films. *J. Phys. Chem. C* **2014**, *118*, 26091−26102.
(24) Savio, L.; Smerieri, M.; Vattuone, L.; Tosoni, S.; Pacchioni, G.; Rocca, M. Interface Oxygen Induced Internal Structures of Ultrathin MgO Islands Grown on Ag (100). *J. Phys. Chem. C* **2020**, *124*, 8834−8842.
(25) Smerieri, M.; Pal, J.; Savio, L.; Vattuone, L.; Ferrando, R.; Tosoni, S.; Giordano, L.; Pacchioni, G.; Rocca, M. Spontaneous oxidation of Ni nanoclusters on MgO monolayers induced by segregation of interfacial oxygen. *J. Phys. Chem. Lett.* **2015**, *6*, 3104−3109.
(26) Savio, L.; Smerieri, M.; Pal, J.; Celasco, E.; Rocca, M.; Vattuone, L. 2D Ni Nanoclusters on Ultrathin MgO/Ag (100). *J. Phys. Chem. C* **2020**, *124*, 482−488.
(27) Gac, W.; Borowiecki, T.; Kowalik, P. Nickel Nanocatalysts for Methane Steam Reforming. *Nanotechnol. Catal. Appl. Chem. Ind. Energy Environ* **2017**, 401−420.
(28) Parmaliana, A.; Arena, F.; Frusteri, F.; Coluccia, S.; Marchese, L.; Martra, G.; Chuvilin, A. Magnesia-supported nickel catalysts: II. Surface properties and reactivity in methane steam reforming. *J. Catal.* **1993**, *141*, 34−47.
(29) Craciun, R.; Shereck, B.; Gorte, R. Kinetic studies of methane steam reforming on ceria-supported Pd. *Catal. Lett.* **1998**, *51*, 149−153.
(30) Kim, H. Y.; Lee, H. M.; Park, J.-N. Bifunctional mechanism of CO2 methanation on Pd-MgO/SiO2 catalyst: independent roles of MgO and Pd on CO2 methanation. *J. Phys. Chem. C* **2010**, *114*, 7128−7131.
(31) Schauermann, S.; Nilius, N.; Shaikhutdinov, S.; Freund, H.-J. Nanoparticles for heterogeneous catalysis: new mechanistic insights. *Acc. Chem. Res.* **2013**, *46*, 1673−1681.
(32) Cadi-Essadek, A.; Roldan, A.; Aparicio-Anglès, X.; De Leeuw, N. H. CO2 and H2 adsorption and reaction at Ni n/YSZ (111) interfaces: a density functional theory study. *J. Phys. Chem. C* **2018**, *122*, 19463−19472.
(33) Mostafa, S.; Behafarid, F.; Croy, J. R.; Ono, L. K.; Li, L.; Yang, J. C.; Frenkel, A. I.; Cuenya, B. R. Shape-dependent catalytic properties of Pt nanoparticles. *J. Am. Chem. Soc.* **2010**, *132*, 15714−15719.
(34) Siakavelas, G. I.; Charisiou, N. D.; AlKhoori, S.; AlKhoori, A. A.; Sebastian, V.; Hinder, S. J.; Baker, M. A.; Yentekakis, I.; Polychronopoulou, K.; Goula, M. A. Highly selective and stable nickel catalysts supported on ceria promoted with Sm2O3, Pr2O3 and MgO for the CO2 methanation reaction. *Appl. Catal., B* **2021**, *282*, 119562.
(35) Rêgo, C. R.; Tereshchuk, P.; Oliveira, L. N.; Da Silva, J. L. Graphene-supported small transition-metal clusters: A density functional theory investigation within van der Waals corrections. *Phys. Rev. B* **2017**, *95*, 235422.
(36) Dong, W.-S.; Jun, K.-W.; Roh, H.-S.; Liu, Z.-W.; Park, S.-E. Comparative study on partial oxidation of methane over Ni/ZrO2, Ni/CeO2 and Ni/Ce−ZrO2 catalysts. *Catal. Lett.* **2002**, *78*, 215−222.
(37) Mayernick, A. D.; Janik, M. J. Methane oxidation on Pd−Ceria: A DFT study of the mechanism over PdxCe1- xO2, Pd, and PdO. *J. Catal.* **2011**, *278*, 16−25.
(38) Caballero, A.; Holgado, J. P.; Gonzalez-delaCruz, V. M.; Habas, S. E.; Herranz, T.; Salmeron, M. In situ spectroscopic detection of SMSI effect in a Ni/CeO 2 system: hydrogen-induced burial and dig out of metallic nickel. *Chem. Commun.* **2010**, *46*, 1097−1099.
(39) Lee, A. F.; Wilson, K. Structure−reactivity correlations in the selective aerobic oxidation of cinnamyl alcohol: in situ XAFS. *Green Chem.* **2004**, *6*, 37−42.
(40) Alayon, E.; Singh, J.; Nachtegaal, M.; Harfouche, M.; van Bokhoven, J. A. On highly active partially oxidized platinum in carbon monoxide oxidation over supported platinum catalysts. *J. Catal.* **2009**, *263*, 228−238.
(41) Johnston, R. L. Evolving better nanoparticles: Genetic algorithms for optimizing cluster geometries. *Dalton Trans.* **2003**, 4193−4207.
(42) Jyakhwo, S.; Serov, N.; Dmitrenko, A.; Vinogradov, V. V. Machine learning reinforced genetic algorithm for massive targeted discovery of selectively cytotoxic inorganic nanoparticles. *Small* **2024**, *20*, 2305375.
(43) Kolsbjerg, E. L.; Peterson, A. A.; Hammer, B. Neural-network-enhanced evolutionary algorithm applied to supported metal nanoparticles. *Phys. Rev. B* **2018**, *97*, 195424.
(44) Esterhuizen, J. A.; Goldsmith, B. R.; Linic, S. Interpretable machine learning for knowledge generation in heterogeneous catalysis. *Nat. Catal.* **2022**, *5*, 175−184.
(45) Li, H.; Jiao, Y.; Davey, K.; Qiao, S.-Z. Data-Driven Machine Learning for Understanding Surface Structures of Heterogeneous Catalysts. *Angew. Chem., Int. Ed.* **2023**, *62*, No. e202216383.
(46) Mou, T.; Pillai, H. S.; Wang, S.; Wan, M.; Han, X.; Schweitzer, N. M.; Che, F.; Xin, H. Bridging the complexity gap in computational heterogeneous catalysis with machine learning. *Nat. Catal.* **2023**, *6*, 122−136.
(47) Rondina, G. G.; Da Silva, J. L. Revised basin-hopping Monte Carlo algorithm for structure optimization of clusters and nanoparticles. *J. Chem. Inf. Model.* **2013**, *53*, 2282−2298.
(48) Li, W.-Z.; Kovarik, L.; Mei, D.; Engelhard, M. H.; Gao, F.; Liu, J.; Wang, Y.; Peden, C. H. A general mechanism for stabilizing the small

sizes of precious metal nanoparticles on oxide supports. *Chem. Mater.* **2014**, *26*, 5475−5481.
(49) Bochicchio, D.; Ferrando, R.; Panizon, E.; Rossi, G. Structures and segregation patterns of Ag−Cu and Ag−Ni nanoalloys adsorbed on MgO (0 0 1). *J. Phys.: Condens. Matter.* **2016**, *28*, 064005.
(50) Bruix, A.; Margraf, J. T.; Andersen, M.; Reuter, K. First-principles-based multiscale modelling of heterogeneous catalysis. *Nat. Catal.* **2019**, *2*, 659−670.
(51) Vines, F.; Gomes, J. R.; Illas, F. Understanding the reactivity of metallic nanoparticles: beyond the extended surface model for catalysis. *Chem. Soc. Rev.* **2014**, *43*, 4922−4939.
(52) Kohn, W.; Sham, L. J. Self-consistent equations including exchange and correlation effects. *Phys. Rev.* **1965**, *140*, A1133.
(53) Hohenberg, P.; Kohn, W. Inhomogeneous electron gas. *Phys. Rev.* **1964**, *136*, B864.
(54) Kresse, G.; Hafner, J. Ab initio molecular dynamics for liquid metals. *Phys. Rev. B* **1993**, *47*, 558.
(55) Kresse, G.; Hafner, J. Ab initio molecular-dynamics simulation of the liquid-metal−amorphous-semiconductor transition in germanium. *Phys. Rev. B* **1994**, *49*, 14251.
(56) Kresse, G.; Furthmüller, J. Efficiency of ab-initio total energy calculations for metals and semiconductors using a plane-wave basis set. *Comput. Mater. Sci.* **1996**, *6*, 15−50.
(57) Kresse, G.; Furthmüller, J. Efficient iterative schemes for ab initio total-energy calculations using a plane-wave basis set. *Phys. Rev. B* **1996**, *54*, 11169.
(58) Perdew, J. P.; Burke, K.; Ernzerhof, M. Generalized gradient approximation made simple. *Phys. Rev. Lett.* **1996**, *77*, 3865.
(59) Blöchl, P. E. Projector augmented-wave method. *Phys. Rev. B* **1994**, *50*, 17953.
(60) Monkhorst, H. J.; Pack, J. D. Special points for Brillouin-zone integrations. *Phys. Rev. B* **1976**, *13*, 5188.
(61) Henkelman, G.; Arnaldsson, A.; Jónsson, H. A fast and robust algorithm for Bader decomposition of charge density. *Comput. Mater. Sci.* **2006**, *36*, 354−360.
(62) Grimme, S.; Antony, J.; Ehrlich, S.; Krieg, H. A Consistent and Accurate Ab Initio Parametrization of Density Functional Dispersion Correction (DFT-D) for the 94 Elements H−Pu. *J. Chem. Phys.* **2010**, *132*, 154104.
(63) Grimme, S.; Ehrlich, S.; Goerigk, L. Effect of the damping function in dispersion corrected density functional theory. *J. Comput. Chem.* **2011**, *32*, 1456−1465.
(64) Wetzel, T. L.; DePristo, A. E. Structures and energetics of Ni24−Ni55 clusters. *J. Chem. Phys.* **1996**, *105*, 572−580.
(65) Rapps, T.; Ahlrichs, R.; Waldt, E.; Kappes, M. M.; Schooss, D. On the Structures of 55-Atom Transition-Metal Clusters and Their Relationship to the Crystalline Bulk. *Angew. Chem., Int. Ed.* **2013**, *52*, 6102.
(66) Piotrowski, M. J.; Ungureanu, C. G.; Tereshchuk, P.; Batista, K. E.; Chaves, A. S.; Guedes-Sobrinho, D.; Da Silva, J. L. Theoretical study of the structural, energetic, and electronic properties of 55-atom metal nanoclusters: a DFT investigation within van der Waals corrections, spin−orbit coupling, and PBE+ U of 42 metal systems. *J. Phys. Chem. C* **2016**, *120*, 28844−28856.
(67) Zeller, R. *Computational Nanoscience: Do It Yourself!*, 1st ed.; John von Neumann Institute for Computing: Jülich, Germany, 2006.
(68) See Supporting Information on top views and planar averages of the electrostatic potential along the z-direction for optimized structures of X55 (X = Ni, Pd, Pt) clusters on various supports: MgO (3L), MgO/Ag, MgO/Ag with oxygen at the interface, MgO/Ag with low-dosage oxygen, and MgO/Ag with high-dosage oxygen and magnetization of Ni atoms vs z-coordinate for MgO/Ag and MgO/O/Ag supports.
(69) Sicolo, S.; Giordano, L.; Pacchioni, G. Adsorption of Late Transition Metal Atoms on MgO/Mo (100) and MgO/Ag (100) Ultrathin Films: A Comparative DFT Study. *J. Phys. Chem. C* **2009**, *113*, 16694−16701.

https://doi.org/10.1021/acs.jpcc.4c04213
J. Phys. Chem. C 2024, 128, 21331−21342